Resolving atomic-scale interactions in non-fullerene acceptor organic solar cells with solidstate NMR spectroscopy, crystallographic modelling, and molecular dynamics simulations

Benjamin R. Luginbuhl, Parth Raval, Tomasz Pawlak, Zhifang Du, Tonghui Wang, Grit Kupgan, Nora Schopp, Sangmin Chae, Sangcheol Yoon, Ahra Yi, et al.

▶ **To cite this version:**

Benjamin R. Luginbuhl, Parth Raval, Tomasz Pawlak, Zhifang Du, Tonghui Wang, et al.. Resolving atomic-scale interactions in non-fullerene acceptor organic solar cells with solidstate NMR spectroscopy, crystallographic modelling, and molecular dynamics simulations. Advanced Materials, 2022, 34 (6), pp.2105943. ⟨10.1002/adma.202105943⟩. ⟨hal-04087965⟩

HAL Id: hal-04087965

https://hal.science/hal-04087965v1

Submitted on 16 May 2023

HAL is a multi-disciplinary open access archive for the deposit and dissemination of scientific research documents, whether they are published or not. The documents may come from teaching and research institutions in France or abroad, or from public or private research centers.

L'archive ouverte pluridisciplinaire **HAL**, est destinée au dépôt et à la diffusion de documents scientifiques de niveau recherche, publiés ou non, émanant des établissements d'enseignement et de recherche français ou étrangers, des laboratoires publics ou privés.

Distributed under a Creative Commons CC BY-NC-ND 4.0 - Attribution - Non-commercial use - No Derivative Works - International License

Resolving atomic-scale interactions in non-fullerene acceptor organic solar cells with solid-state NMR spectroscopy, crystallographic modelling, and molecular dynamics simulations

Benjamin R. Luginbuhl, Parth Raval, Tomasz Pawlak, Zhifang Du, Tonghui Wang, Grit Kupgan, Nora Schopp, Sangmin Chae, Sangcheol Yoon, Ahra Yi, Hyo Jung Kim, Veaceslav Coropceanu, Jean-Luc Brédas, Thuc-Quyen Nguyen, and G. N. Manjunatha Reddy**

B. R. Luginbuhl, Z. Du, N. Schopp, S. Chae, S. Yoon, Prof. T-Q. Nguyen
Center for Polymers & Organic Solids, Department of Chemistry and Biochemistry, University of California Santa Barbara, Santa Barbara, California 93106, United States.
E-mail: quyen@chem.ucsb.edu

P. Raval, Dr. G. N. M. Reddy
University of Lille, CNRS, Centrale Lille Institut, Univ. Artois, UMR 8181, Unité de Catalyse et Chimie du Solide, F-59000, Lille, France.
E-mail: gnm.reddy@univ-lille.fr

Dr. T. Pawlak
Centre of Molecular and Macromolecular Studies, Polish Academy of Sciences, Sienkiewicza 112, 90-363 Lodz, Poland.

Dr. T. Wang, Dr. G. Kupgan, Prof. V. Coropceanu, Prof. J.-L. Brédas
Department of Chemistry and Biochemistry, University of Arizona, Tucson, Arizona 85721, United States.

A. Yi. Prof. H. J. Kim
Department of Organic Material Science and Engineering, School of Chemical Engineering, Pusan National University, Busan 46241, Republic of Korea.

Keywords: *organic semiconductors, morphology, NFA solar cells, bulk heterojunction, self-assembly, packing interactions, polymers*

Abstract

Fused-ring core non-fullerene acceptors (NFAs), designated "Y-series", have enabled high-performance organic solar cells (OSCs) achieving over 18% power conversion efficiency (PCE). Since the introduction of these NFAs, much effort has been expended to understand the reasons for their exceptional performance. While several studies have identified key optoelectronic properties that govern high PCEs, little is known about the molecular level origins of large variations in performance, spanning from 5 to 18% PCE, *e.g.*, in the case of PM6:Y6 OSCs. Here, we introduce a combined solid-state NMR, crystallography, and molecular modelling approach to elucidate the atomic-scale interactions in Y6 crystals, thin films, and PM6:Y6 bulk heterojunction (BHJ) blends. We show the Y6 morphologies in BHJ blends are not governed by the morphology in neat films or single crystals. Notably, PM6:Y6 blends processed from different solvents self-assemble into different structures and morphologies, whereby the relative orientations of the sidechains and end groups of the Y6 molecules to their fused-ring cores play a crucial role in determining the resulting morphology and overall performance of the solar cells. The molecular-level understanding of BHJs enabled by this approach will guide the engineering of next-generation NFAs for stable and efficient OSCs.

1. Introduction

Single-junction organic solar cells (OSCs) based on non-fullerene acceptors (NFAs) have recently seen dramatic increases in performance, with devices currently achieving over 18% power conversion efficiency (PCE).[1,2] A major factor in this rise in performance has been credited to the introduction of the "Y-series" NFAs, in particular the molecule Y6, which enabled a significant leap forward in OSCs to achieve over 15% PCE in 2019.[3,4] As a consequence of these impressive results, an explosion of work is currently underway to i) understand the fundamental physics that govern the high performance of Y6 and its derivatives in OSCs,[2,5–31] ii) unravel the role of morphology and packing interactions on the device performance, and iii) extend this knowledge to design and develop NFA-based bulk heterojunction (BHJ) blends that achieve efficient OSCs with record PCEs.[8,32,33]

Central to the performance of OSCs is the (BHJ) morphology – an interpenetrating network of p-type donor (D) and n-type acceptor (A) organic semiconductors – that facilitates free charge carrier generation and transport.[34–37] The "soft" chemistry associated with the BHJ morphology, which relies on molecular self-assembly of donor-acceptor moieties driven by multiple noncovalent interactions, manifests in different degrees of heterogeneity in compositions, structures, and optoelectronic properties. The morphology can be further modified by the choice of solvent, the use of solvent additives to modulate the solvent evaporation rate during the film formation process, the temperature of the solution and substrate, and by post-processing techniques such as solvent-vapor and thermal annealing.[38–41] In addition, the properties of the BHJ are influenced heavily by the chemical nature of the materials used, including the molecular weights (for polymers), aggregation behaviors, relative solubilities, to name a few.[42] The combination of all these factors leads to a complex web of interdependent properties, which ultimately determine the overall performance of BHJ OSCs.[37]

To date, a complete picture of the processes that govern BHJ morphology formation has been difficult to achieve and predict. The use of approaches that combine X-ray scattering and diffraction, microscopy, and computational modelling can elucidate the correlations between morphology and bulk properties of BHJ OSCs in some cases, albeit with some amount of speculation still required to generalize the findings to other NFA-based OSCs. Specifically, grazing-incidence wide-angle X-ray scattering (GIWAXS) measurements can resolve π-π stacking distances between molecules in thin films and orientations of the molecules with respect to a glass substrate that can be correlated to optoelectronic properties;[43,44] however, this technique only probes crystalline regions of the BHJ blends. Additionally, resonant soft X-ray scattering (RSoXS) can be used to measure the domain sizes of donors and acceptors and phase purity in a BHJ morphology. When these techniques are coupled with scanning and transmission electron microscopy (SEM and TEM), nano-scale resolution of the surface BHJ layer may be achievable. However, one aspect that each of these techniques is missing is the ability to resolve differences in the atomic-scale interactions between and within D and A molecules in thin films. To this end, solid-state NMR (ssNMR) spectroscopy has provided excellent insights for organic semiconductors and BHJ materials, allowing atomic-scale interactions to be resolved.[5,45–48,42,49–53] Further, when used in conjunction with X-ray scattering and modelling techniques, ssNMR can identify specific atomic-scale morphologies in organic semiconductors, including BHJ blends.[46,54–59] Despite the resolving power of this combination of techniques, it has seldom been applied to the characterization of NFA-based organic solar cells, largely due to the challenges associated with interpreting NMR signals resulting from chemically similar donor and acceptor building blocks along with the relatively large degrees of disorder associated with BHJs.[5,42,60] Here, we demonstrate a combined approach to overcome these challenges to obtain a more

complete understanding of the morphological differences in Y6 based OSCs prepared with different processing conditions.

The donor polymer PM6 has been used extensively in conjunction with Y6 to produce high-performing OSCs,[3,10] though the PCEs of PM6:Y6 OSCs at the laboratory scale have been shown to vary from approximately 5% to over 18% depending on the processing conditions, the structures and properties of the donor and acceptor.[8,10,42] While several experimental and modelling studies have focused on understanding the device physics and morphology that lead to the high performances, few have investigated the reasons for this large range of performances, and in particular why some processing conditions favor beneficial morphologies, while others lead to poor morphologies with relatively low overall performance. There are several unanswered questions regarding exactly what causes an efficient morphology to form and be preserved in BHJ blends. For example, Y6 films processed from chloroform (CF) or chlorobenzene (CB) solvents differ dramatically in their morphology:[10] CB-processed Y6 films adopt a mixed polycrystalline morphology with no clear preferred orientation relative to the substrate, whereas in CF, Y6 orients face-on to the substrate. These morphological differences were correlated to the different performances in PM6:Y6 solar cells, with CB-processed devices achieving only 12% PCE and CF devices achieving up to 16.9%, depending on the thermal annealing conditions used. In another report, neat Y6 films and PM6:Y6 blend films prepared from CF exhibited few morphological differences (as determined from X-ray scattering, TEM, and AFM); though there were notable differences in PCE values between PM6:Y6 solar cells with and without thermal annealing (13.88% versus 14.79%), with annealed films leading to higher PCEs.[9] In addition, it was found that the conformational rigidity of Y6, caused by the strong coupling between the core and end groups, leads to a high degree of uniformity in the films, suggesting a morphology favorable for charge transport.[61] This finding was corroborated by X-ray scattering measurements and analyses

that show Y6 maintains a similar morphology from neat films to blends, and demonstrates efficient charge transport in both cases.[9] Furthermore, single crystals of Y6 showed different packing interactions despite being prepared in nominally similar conditions.[2,6,9,11] To this end, the difficulty in developing a general trend and an intuitive understanding of structure-processing-property relationships endures due to the intrinsic complexity of BHJ blends that ultimately manifest the device properties.

In this study, we introduce a protocol to gain an atomic-level insight into the structure-processing-property relationship in PM6:Y6 BHJ solar cells. Our approach combines ssNMR, crystallography modelling and molecular dynamics (MD) simulations to elucidate the key structure-directing interactions that govern bulk morphologies in Y6 thin films. Specifically, short-range (sub-nanometer) structures and intermolecular interactions in neat materials and BHJ blends are analyzed by multinuclear (^{1}H, ^{13}C, and ^{19}F) 1D and 2D ssNMR spectroscopy. While PM6 exhibits identical morphology in neat and blend films, Y6 shows different morphological features in neat and blends processed from different solvents, which is corroborated by periodic density functional theory (DFT) calculations and MD simulations of previously reported Y6 single crystals. Building upon the fundamental understanding of molecular self-assembly of Y6 molecules in single crystals, we correlate and compare the morphology of Y6 and PM6 thin films and their blends to understand the underlying reasons for different chemical environments, and thus the range of PCEs from 9.7 to 15.0% associated with PM6:Y6 BHJ solar cells cast from three solvents, CF, CB, and *o*-xylene (*o*-XY). The work also highlights specific intermolecular interactions that are important in pristine Y6 and in PM6:Y6 films.

2. Results and Discussion

2.1 Solar Cell Fabrication and Characterization

We first fabricated inverted-architecture BHJ OSCs (ITO/ZnO/active layer/MoO_x/Ag) from blends of PM6 and Y6 in three different solvents: chloroform, chlorobenzene, and *o*-xylene. For the CF and *o*-XY solutions, 1-chloronapthalene (1-CN) additive was added to form a solution with 0.5% 1-CN by volume, following optimization procedures from previous work.[5,53] The weight ratio between PM6 and Y6 was kept constant at 1:1.2 and the total solid concentration was 16 mg mL^{-1}. Further details regarding the device fabrication procedure are given in the Supporting Information. **Figure 1** shows the chemical structures of PM6 and Y6, the energy levels of the materials used for the inverted architecture OSCs, as well as a schematic representation of the device structure.

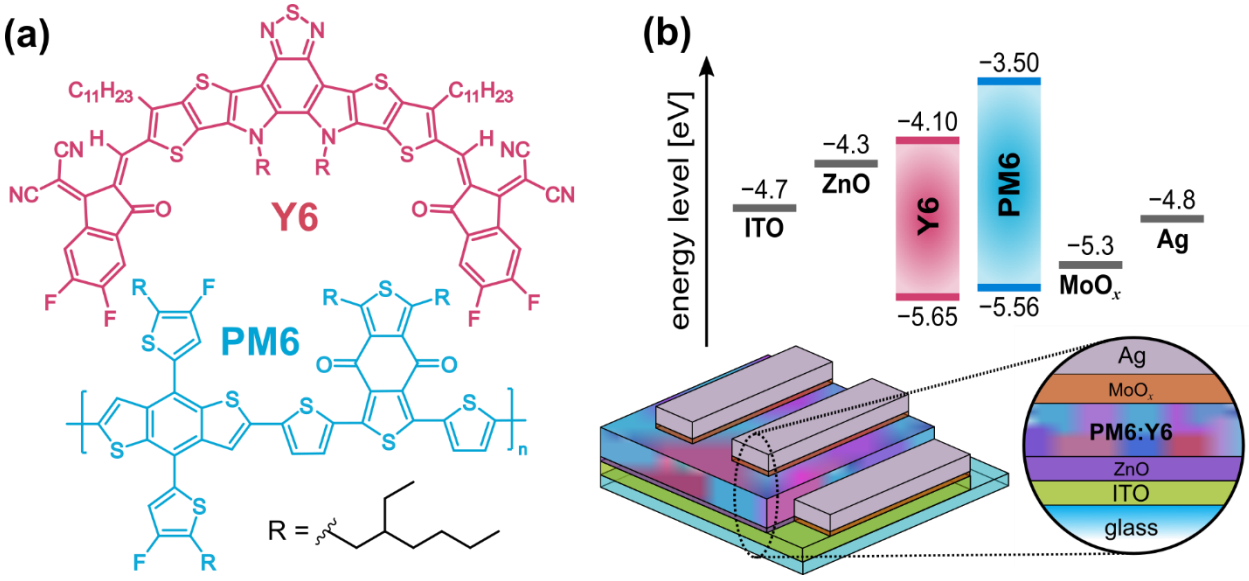

Figure 1. (a) Chemical structures of PM6 and Y6. **(b)** Energy level diagram of the inverted BHJ devices used in this study and a schematic representation of the organic solar-cell architecture.

Next, the current-density versus voltage (*J*-*V*) behavior of the OSC devices under 1-sun (AM1.5G) illumination was measured. The devices prepared from CF showed the best

performance, with a higher open-circuit voltage (V_{OC}), short-circuit current density (J_{SC}), and fill factor (FF) compared to devices prepared from CB and *o*-XY solutions. The average performance metrics for 10 devices prepared from each solution are summarized in **Table 1**, and the J-V characteristics of representative devices from each solvent are shown in **Figure S2** in the Supporting Information. The performance of these OSCs agrees with previously reported results in the literature[5,9,10,53] (a comprehensive list of different PCEs exhibited by PM6:Y6 based OSCs are given in Ref. 8, Tables 3 and 4) and provide a basis to compare the morphological differences between the blends from different solvents. For PM6:Y6 blends processed from CF, CB, and *o*-XY solvents, little morphological differences were observed from GIWAXS and AFM (Supporting Information, **Figures S3-S5**); however, there were still marked differences in performance, *i.e.*, in the V_{OC}, J_{SC} and FF values.

Table 1. Performance metrics for PM6:Y6 solar cells made from three different solvents. Values are averages from at least 10 devices with their standard deviations.

Solvent	$\boldsymbol{V_{OC}}$ [V]	$\boldsymbol{J_{SC}}$ [mA cm^{-2}]	$\boldsymbol{FF}$ [%]	$\boldsymbol{PCE}$ [%]
CF[a)]	0.825 ± 0.003	25.50 ± 0.7	72.0 ± 2.0	15.0 ± 0.4
CB	0.744 ± 0.006	20.32 ± 0.2	67.0 ± 2.0	10.45 ± 0.26
o-XY[a)]	0.790 ± 0.003	18.44 ± 0.2	67.0 ± 1.0	9.66 ± 0.25

a) with 0.5% (v/v) 1-CN additive.

2.2 Resolving atomic-scale interactions in PM6 and Y6 thin films

The pertinent fundamental question is whether different packing interactions in D and A moieties are responsible for the large variations in PCE values. Given the heterogeneous chemical nature of BHJ blends, establishing processing-structure-property relationship can only be performed by gaining access to high-resolution techniques that allow the inter- and intramolecular interactions to

be characterized at the atomic level. We demonstrate a combined ssNMR, crystallography modelling and all-atom MD simulations (also referred to as NMR crystallography) to gain insight into the structure-processing-property relationship in PM6:Y6 OSCs. **Figure 2** illustrates how this approach enables key structure-directing interactions in PM6, Y6 and PM6:Y6 blends to be resolved and distinguished at atomic-scale resolution. Notably, the iteration step that interconnects experimental characterization, modelling and structure-property relationships is central to the overall outcome and reliability of the proposed approach. For example, better agreement between calculations and experimental data can be obtained using interatomic distances from crystal structures or ssNMR experiments. These data can be attained for a range of NFAs and donor polymers and their blends. A detailed description of the different steps involved, the generality of the approach, and the consistency of the results for this experiment is given in the below sections and in the Supporting Information (**Section 5**).

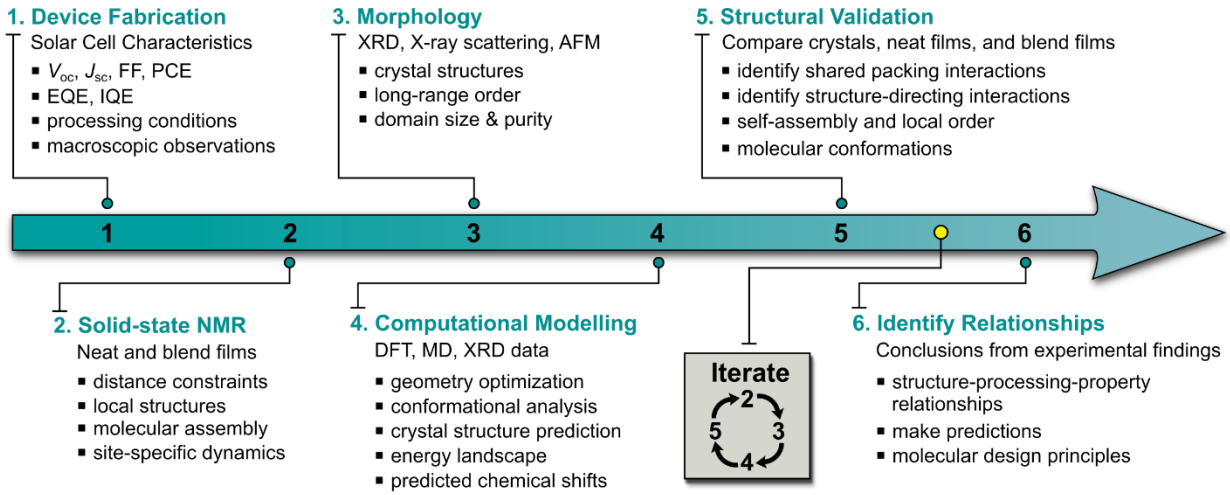

Figure 2. A schematic of the combined ssNMR and crystallgoraphy modelling approach for understanding structure-processing-performance relationships in NFA-based OSCs.

We begin with ssNMR to investigate the local bonding environments of ^{1}H, ^{13}C, and ^{19}F sites in Y6, PM6, and PM6:Y6 blend films processed using the same conditions as the OSCs. The materials for ssNMR were prepared by spin coating thin films of each material onto cleaned glass

substrates in an inert-atmosphere glovebox (see the Supporting Information, **Table S1** for solution details). First, we analyzed the ^{19}F magic-angle spinning (MAS) NMR spectra of neat PM6, Y6, and PM6:Y6 **(**1:1.2, g/g) blends cast from CF, CB and *o*-XY solvents. These spectra are shown in **Figure 3**. Interestingly, we find that PM6 shows a single chemical environment for its ^{19}F atoms, as evidenced by a single peak centered at –131 ppm (**Figure 3a-c**), regardless of the solvent or whether it is blended with Y6 (**Figure 3g-i**). This indicates that the local structures of the fluorinated pendant units of PM6 are not influenced by solvent processing, which we further ensure by the detailed 1D and 2D ^{1}H and ^{13}C NMR analysis discussed below. It can therefore be reasoned that the PM6 donor polymer (M_n = 43.7 kDa with less than 1% low molecular weight fraction) has little impact on the large variation in the PCE values shown in **Table 1**, leading us to focus our efforts on the morphology and packing interactions of Y6.

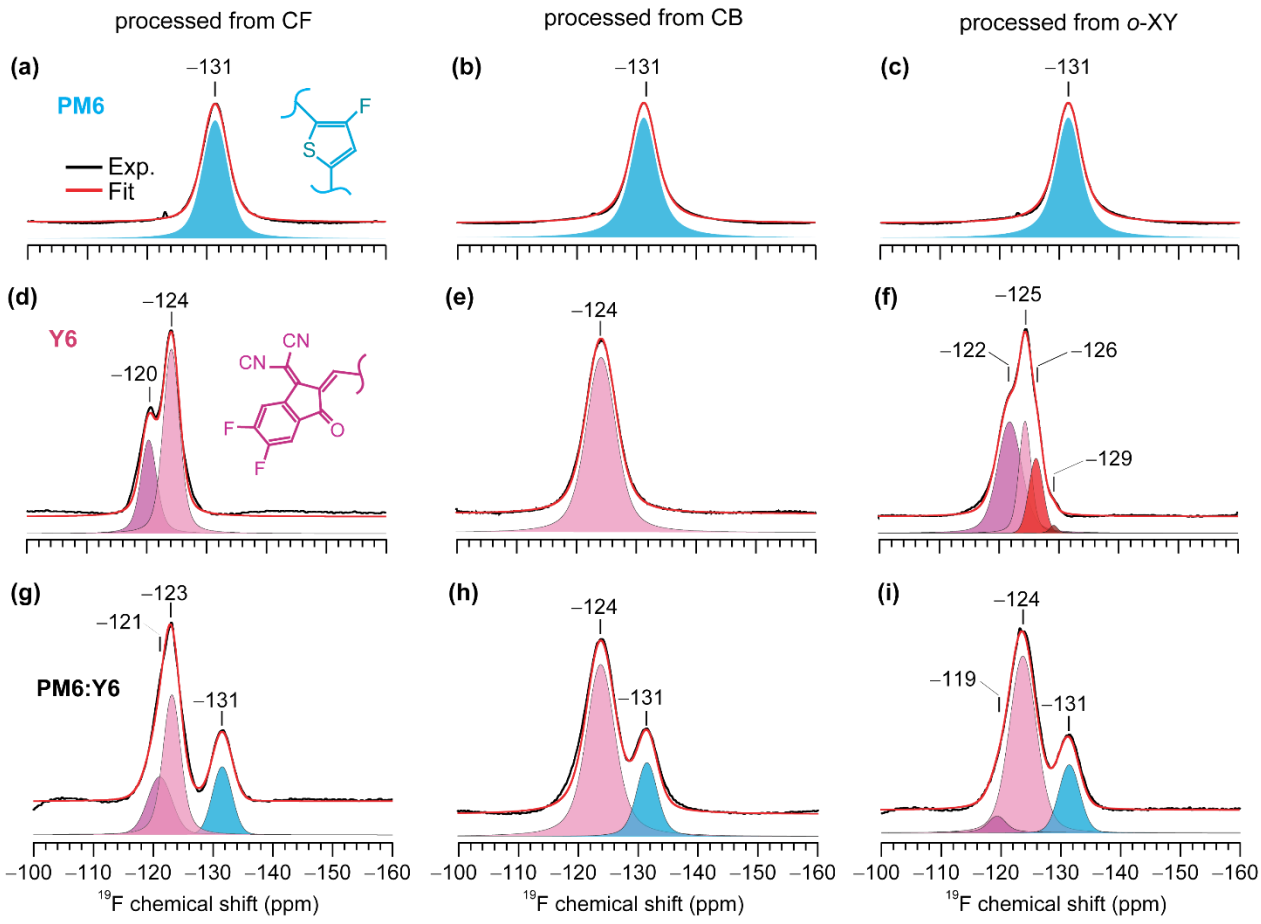

Figure 3. Solid-state 1D ^{19}F NMR spectra of **(a-c)** PM6, **(d-f)** Y6, and **(g-i)** PM6:Y6 BHJ films processed from CF, CB, and *o*-XY solvents. ^{19}F signals correspond to PM6 and Y6 moieties as indicated. Peak intensities are deconvoluted to identify signals from distinct ^{19}F environments that contribute to the overall spectral shapes.

In contrast to PM6 films, the fluorinated end groups of Y6 films show different solid-state ^{19}F signals depending on which solvent the film was cast from. Films cast from CF show two distinct signals centered at −120 and −124 ppm, as shown by the deconvoluted spectra in **Figure 3d**, whereas Y6 prepared from CB shows a single peak centered at −124 ppm (**Figure 3e**). In neat films of Y6 cast from *o*-XY, four separate ^{19}F signals are observed, with peaks centered at −122, −125, −126, and a small shoulder peak at −129 ppm (**Figure 3f**). PM6:Y6 blends (**Figure 3g-i**) prepared from CB and *o*-XY solutions have similar spectra, with a dominant peak from Y6 centered at −124 ppm; *o*-XY films retain a minor component peak centered at −119 ppm. In the blend processed from CF, however, Y6 retains its characteristics from the neat films, with only minor changes in the relative intensities and positions of the two original signals. The molecular-level changes in the Y6 acceptor morphology in neat films and blends are intriguing as they could be related to the significant differences in the charge carrier properties and device characteristics. These results suggest that a reason for the difference in OSC performance between these blends could be related to the presence of distinct chemical environments around the end groups of Y6, which are observed in thin films cast from CF (the solvent that leads to the highest performance), but not in CB or *o*-XY. The question then arises whether the self-assembly and morphology of Y6 is solely influenced by the fluorinated end groups or whether other inter- and intramolecular interactions also contribute to such substantial differences in the bulk photovoltaic properties.

A more complete picture of the different inter- and intramolecular interactions in neat compounds and blends can be obtained by analyzing the local environments of ^{1}H and ^{13}C sites in the thin films. In doing so, we compare 1D ^{1}H and ^{13}C spectra of neat PM6, Y6, and PM6:Y6 blends processed from CF, CB and *o*-XY solvents (Supporting Information **Figures S6 and S7**). While the ^{1}H NMR spectra of neat PM6 films show nearly identical line shapes for each solvent, Y6 films show different peaks and line shapes, particularly in the aromatic region, which is consistent with the 1D ^{19}F NMR results and analysis. It is noteworthy that the $^{19}F \rightarrow {}^{13}C$ cross-polarization (CP) NMR experiments enable the signals associated with ^{13}C sites in the vicinity of fluorine atoms in PM6 and Y6 molecules to be resolved. A comparison of $^{13}C\{^{19}F\}$ CP-MAS spectra of Y6, PM6 and PM6:Y6 blends processed from different solvents is given in Supporting Information (**Figure S8**). Although the $^{13}C\{^{19}F\}$ signals of the PM6 polymer overlap with the analogous signals from Y6 molecules in the PM6:Y6 blend processed from CF, the relatively broad distribution of signals in neat Y6 film compared to the PM6:Y6 blend (**Figure S8a,** red and black spectra) further confirms the changes in the local environments of Y6 end groups. For PM6:Y6 blends processed from different solvents, subtleties in the distributions of $^{13}C\{^{19}F\}$ signals in the range of 151-157 ppm indicate changes in the local structures of Y6 end groups (Supporting Information, **Figure S8b)**, however, these data alone do not provide any information on the inter- and intramolecular backbone-sidechain interactions in neat Y6 films and in PM6:Y6 BHJ blends. We also carried out 2D ^{1}H-^{1}H Double-Quantum–Single-Quantum (DQ-SQ) correlation NMR and 2D ^{1}H-^{13}C heteronuclear correlation (HETCOR) experiments, which enable the 2D peaks corresponding to through-space dipolar coupled ^{1}H-^{1}H pairs and ^{1}H-^{13}C pairs at sub-nanometer distances to be resolved. A detailed analysis of the 2D DQ-SQ and HETCOR spectra for the PM6 macromolecules (Supporting Information, **Figures S9** and **S10**) allows the inter- and intramolecular interactions to be elucidated. In particular, 2D ^{1}H DQ-SQ analysis corroborates that

the PM6 films processed from CF, CB, and *o*-XY solvents exhibit identical local structures in neat compounds and blends (Supporting Information **Figures S10, S18, S19**), indicating that the choice of solvent does not impact the local morphology of PM6. However, it does affect that of Y6 (as will be discussed in greater details in the subsequent sections), confirming that the acceptor morphology is primarily responsible for the different device properties of PM6:Y6 solar cells shown in **Table 1**. This result prompts us to systematically investigate the different packing interactions in Y6 crystals processed from different solvents using an NMR crystallography approach.

2.3 Y6 Packing Interactions in Crystals Probed by NMR Crystallography

NMR crystallography combines theory and experiment to resolve structures and packing interactions in (semi-)crystalline and powder compositions of small molecules including organic semiconductors,[54,55,58,62] and to characterize the molecular self-assembly process.[63,64] In each of the three Y6 crystals investigated,[6,9,11] which we designate as Form I[9], Form II[6], and Form III[11] for convenience, crystals were grown via solvent vapor diffusion from a solution of Y6 into an orthogonal solvent. Form I was obtained from a dibromomethane solution of Y6 diffusing into acetone, Form II from CF into ethanol, and Form III from CF into isopropanol. In all cases, the unit cells contain crystallographically independent molecules, denoted as "A" and "B" (**Figure 4)**. Each crystal exhibits different π-π stacking interactions, void fractions, self-assembly, molecular conformations, and local structures of the end groups and sidechains (Supporting Information, **Figures S11** and **S12**, **Tables S2-S4**), indicating that the Y6 crystal morphology is sensitive to solution processing. It is noteworthy that the Y6 crystal structures resolved from X-ray diffraction have different side chain lengths and compositions due to the ambiguity involved in solving a full crystal structure that contains long, unsaturated hydrocarbon chains. However, the crystal

structures contain valuable information about the relative packing distances and orientations of the Y6 core and end groups, and this information can be used to ascertain whether these molecular packing motifs are present in Y6 thin films.

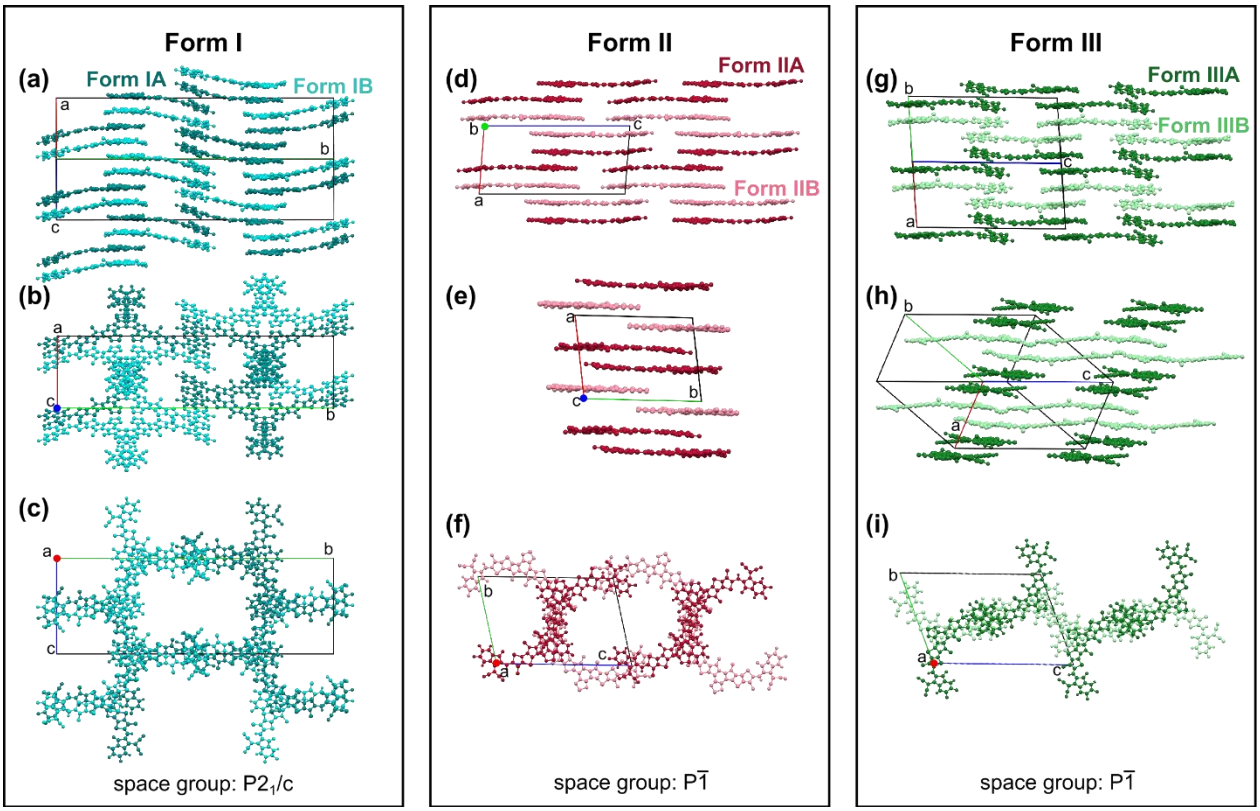

Figure 4. Crystallographically distinct molecules "A" and "B" in full crystals of **Y6** grown from dibromomethane - Form I **(a-c)**,[9] from an ethanol/chloroform mixture - Form II **(d-f)**,[6] and from chloroform/isopropanol mixture - Form III **(g-i)**.[11] The alkyl sidechains have been omitted for clarity.

To gain insight into the influence of different intermolecular packing interactions on the chemical shifts observed by ssNMR, we compare the DFT-calculated NMR chemical shifts of Y6 crystal structures with experimental NMR chemical shifts of Y6 thin films (**Figure 2**, iteration of steps 2-4). If the calculated chemical shifts of the atoms in the single crystals are similar to those measured in Y6 thin films, this means the molecular packing in thin films is similar to that of the

Y6 single crystal. Each crystal structure obtained from previous literature was geometry optimized using a gauge including projector augmented wave (GIPAW) DFT approach, which accounts for periodic boundary conditions to calculate the magnetic resonance properties of the molecules in crystals.[65–67] To compare the DFT results for the different crystal packing motifs and for the individual monomers in each cell, a consistent labeling schema, shown in **Figure 5a**, was used to identify chemical shifts of the individual atoms, which were then visualized and analyzed using the MagresView and MagresPython software tools.[65] A comparison of DFT calculated chemical shifts and experimental ^{1}H, ^{13}C, ^{15}N and ^{19}F NMR spectra is shown in Supporting Information (**Figures S13** and **S14, Table S5).**

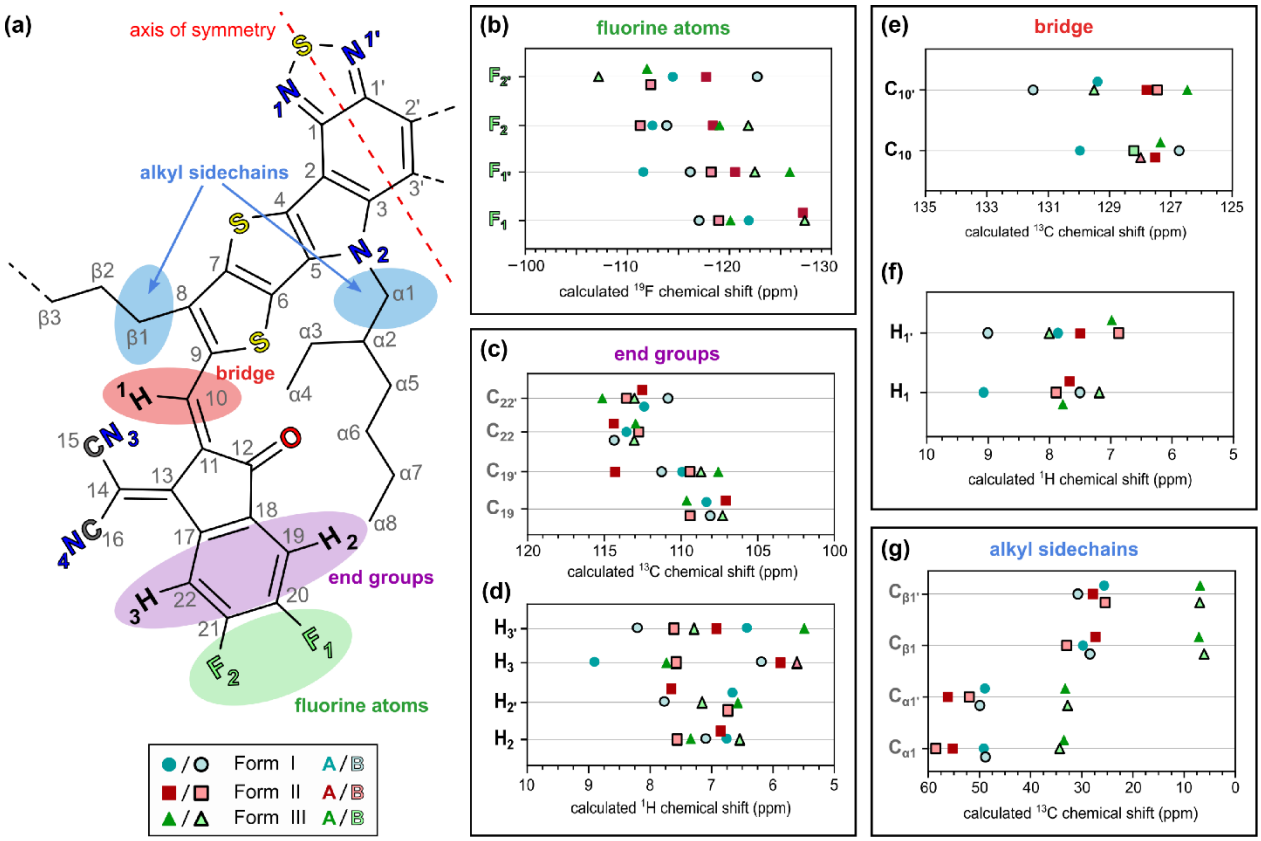

Figure 5. (a) Atomic labelling schema for GIPAW-DFT calculated NMR chemical shifts. The labels for atoms with the same symmetry about the central axis have been given a prime (′) designation. The plots in (b-g) correspond to: (b) the ^{19}F sites in the end goups, (c) the protonated

^{13}C sites in the end groups and (d) the 1H atoms bonded to these carbons; (e) the bridging ^{13}C and (f) ^{1}H sites; (g) the first carbon atoms on each alkyl sidechains attached to the fused-ring core. Atoms with similar chemical shifts (ppm) have been vertically offset from the horizontal axes for clarity. The data shown are tabulated in the Supporting Information, **Table S5**.

In general, it is worth noting that the large range of chemical-shift values for each atom between the different crystal structures for the same Y6 backbone moiety is attributable to different local structures of end groups and sidechains. For example, changes in the DFT calculated ^{19}F chemical shifts (labelled F_1 and F_2 in **Figure 5a,b**) corroborate the different distributions of experimental ^{19}F chemical shifts shown in **Figure 3d-f**. Next, it is instructive to view the patterns in chemical shifts for certain ^{13}C and ^{1}H atoms in Y6, namely the protonated aromatic carbons in the end groups (C_{19} and C_{22}, H_2 and H_3, **Figure 5c, d**), the bridging =CH– between the core and end groups (C_{10}, H_1, **Figure 5e,f**), and the first carbon atom in each alkyl sidechain adjacent to the core ($C_{\alpha 1}$ and $C_{\beta 1}$, **Figure 5g**). As was found in the calculated chemical shifts of the other atoms above, we again see notable differences between the ^{19}F, ^{13}C, and ^{1}H chemical shifts for A and B molecules in different crystal structures (Supporting Information, **Table S5**). In addition, the pyrrolo-nitrogen atoms (labelled N_2 and $N_{2'}$ in **Figure S13**) in crystal Forms I and II have chemical shifts are in the range of 129-140 ppm, whereas the equivalent atoms in the Form III structure are shifted to 110-120 ppm. It is also worth noting that the packing differences create starkly different chemical environments for atoms that are symmetrically positioned at the two ends within a monomer, *i.e.*, the chemical-shift differences between the A and B molecules in **Figure 5b-g**.

The different distributions of DFT calculated chemical shifts can be ascribed to different inter- and intramolecular interactions and the cooperative interplay between them. To explore this further, we investigated the impact of conformational tilts of the end groups (*i.e.*, the dihedral angle

between the core and end groups) and the sidechain structures on the supramolecular order of Y6 molecules (Supporting Information, **Table S4**). While the GIPAW-DFT analysis indicates that Y6 crystal structures exhibit different packing interactions, the different sidechain structures associated with these Y6 crystals makes it difficult to compare the role of sidechains on the backbone order and packing interactions. For example, a shift in the DFT-calculated ^{13}C and ^{1}H chemical shifts in **Figure 5g** (green triangles *vs.* cyan/red triangles have an offset of up to 20 ppm) could be attributed to the differences in sidechain lengths between the Y6 crystal structures, *e.g.*, Forms I and II have multiple carbon atoms in their linear sidechains, while Form III has only a single methyl group. To gain further insight and clarification on sidechain-backbone interactions, we now turn to molecular dynamics simulations.

2.4 Molecular Dynamics Simulations of Sidechain Distributions in Y6

All-atom molecular dynamics (AA-MD) simulations of Y6 crystals can shed light into the specific interactions between the core, bridge, and end group moieties with the aliphatic sidechains. Starting from GIPAW-DFT optimized periodic structures of the Y6 backbones, the linear (undecyl, attached at $C_8/C_{8'}$, see Figure 5a) and branched (2-ethylhexyl, attached at $N_2/N_{2'}$) sidechains were attached to the core. Then, MD simulations were performed using the NVT (*i.e.*, constant number of molecules, volume, and temperature) ensemble for 60 ns at a temperature of 300 K. The lattice parameters were fixed while the atoms in the Y6 backbones and sidechains were allowed to fully relax. Further details of the MD simulations are given in Supporting Information (**Section 5.5**).

Figure 6 shows the radial distribution functions (RDFs), $g(r)$, for the bridging carbon atoms ($C_{10/10'}$) and the protonated carbons in the end groups ($C_{19/19'}$ and $C_{22/22'}$) with respect to hydrogen atoms in the sidechains (as shown in **Figure 6a**). Two separate cases were analyzed: i) exclusively intermolecular distances (**Figure 6c-e**) and ii) both intermolecular and intramolecular distances (**Figure 6f-h**). Considering intermolecular sidechain-end group distances, we find that the RDFs

of Form I are distinct relative to those of Forms II and III. Form I displays a larger number of interactions between C_{22} and ^{1}H atoms in the branched sidechains. The intermolecular RDF patterns in Forms II and III are similar, except for the presence of a peak around 2.8 Å in Form II (**Figure 6d**, dashed blue line) indicating additional interactions between C_{22} and ^{1}H atoms in the linear sidechains of neighboring molecules. These observations are also reflected in the RDF data including both intermolecular and intramolecular interactions. The =CH- (C_{10}, H_1) group in the bridging position appears to be in close proximity with the linear alkyl sidechains attached to the bithiophene groups of the fused-ring core, which suggests the presence of co-planar arrangements of Y6 molecules. Indeed, such intermolecular interactions between end groups and sidechains play an important role in enhancing backbone planarity and stabilizing the overall Y6 morphology.[2]

Further, we investigated the distribution of the angles formed between the end groups and the different alkyl sidechains. These data are summarized in **Figure S15** in the Supporting Information. We find significant differences in these angle distributions among the different crystal forms. Forms I and III have single distributions (**Figure S15f-h**), for which a majority of the linear sidechains and the longer segments (*n*-butyl) of the branched sidechains are oriented nearly parallel to the aromatic plane of the end groups (*i.e.*, the vectors related to these sidechains adopt orientations close to ~90° with respect to the vectors normal to the end groups). In contrast, Form II shows a bimodal distribution of the angles between the vector normal to the end group and the vector related to the *n*-butyl segments of the branched sidechains, indicating the presence of two distinct preferred orientations. Also, while all forms show bimodal distributions for the angles between the shorter segment (ethyl) of the branched sidechains and the vectors normal to the end groups, Form II displays a much broader range, with all angles between 0 and 90 degrees represented (**Figure S15j**); Forms I and III, on the other hand, have no angles greater than 70 degrees (**Figure S15i,k**). In agreement with the conclusions drawn from the GIPAW-DFT

calculations, the variations in the RDF patterns and angle distributions confirm that the Y6 polymorphs adopt different local structures between end groups and alkyl sidechains; thus, the different crystalline structures lead to different local environments, which we anticipate to be a key element contributing to the observed differences in device performance.

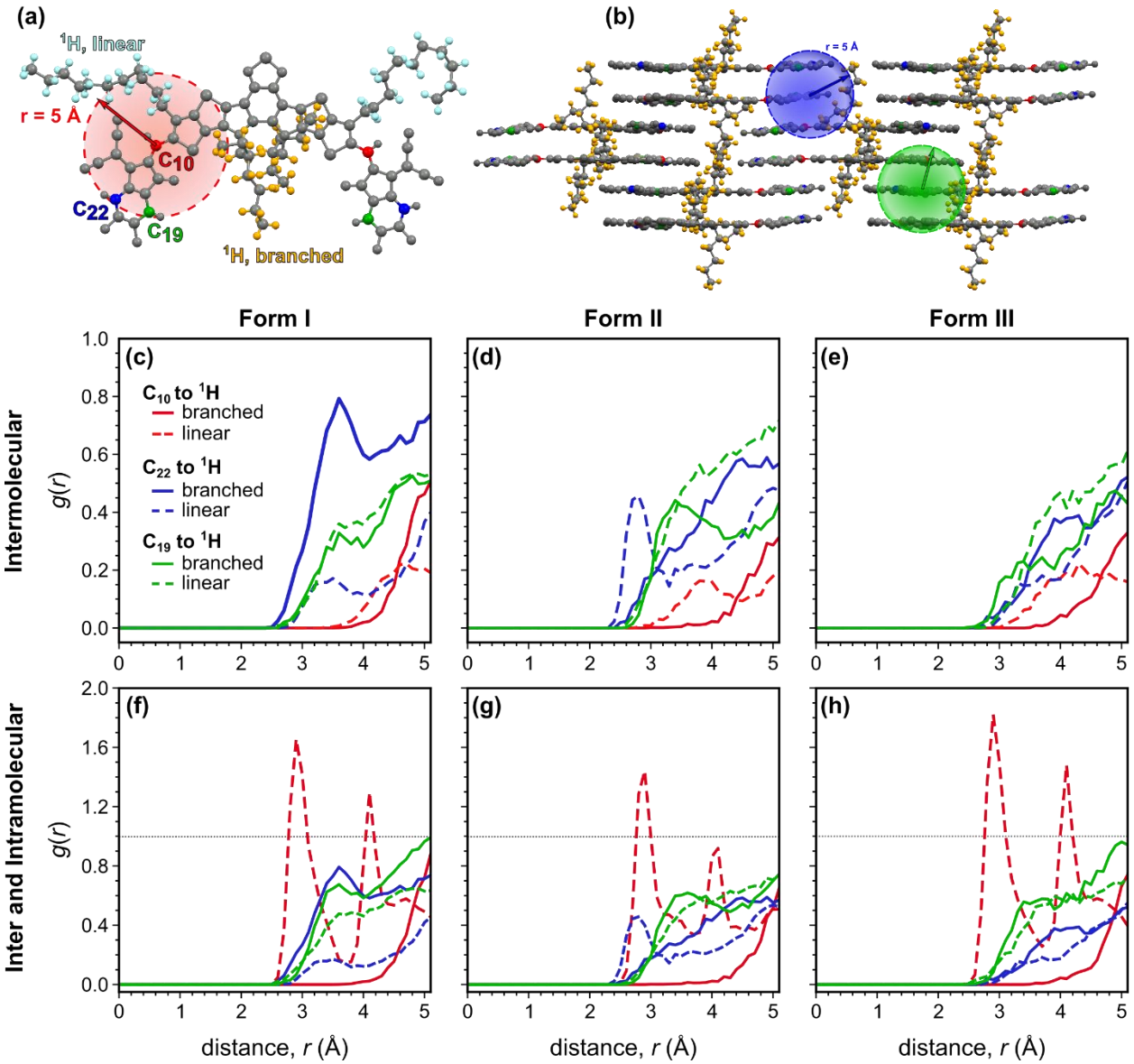

Figure 6. Radial distribution functions for selected carbon atoms and sidechain hydrogens of Y6 molecules in Form I, Form II, and Form III. The GIPAW-optimized structures were used as the starting configurations of the MD simulations. **(a)** illustrates the selected carbon atoms (C_{10}, C_{19}, and C_{22}); **(b)** shows an example of a 5-Å radius centered on the end group carbons. Only

intermolecular interactions are displayed for Forms I, II, and III in **(c)**, **(d)**, and **(e)**, respectively, while total interactions (*i.e.*, including intramolecular interactions) are displayed in **(f)**, **(g)**, and **(h)**. The black dotted lines at $\boldsymbol{g(r) = 1}$ in **(f)**, **(g)**, and **(h)** serve as a guide to compare the values of $\boldsymbol{g(r)}$ with **(c)**, **(d)**, and **(e)**.

2.5 Y6 Packing Interactions in Thin Films Probed by NMR Crystallography and 2D NMR

The above NMR crystallography study provides an excellent basis to corroborate the experimental 2D ssNMR data of neat Y6 films and PM6:Y6 BHJ blends processed from different solvents. We position this analysis (GIPAW-DFT chemical shifts, RDFs of Y6 crystals and 2D ssNMR results) in the context of identifying and distinguishing the changes in local structures, self-assembly and interactions between the end groups and sidechains of Y6 molecules in crystals, thin films and blend films processed from different solvents (**Figure 2**, step 5). Of the aforementioned analysis of three different Y6 crystals, we consider Form II (CF-processed) to compare crystal versus thin-film morphology. For the Y6 film processed from CF, the 2D HETCOR spectra in **Figure 7a** were acquired with 0.1 ms and 4 ms cross-polarization (CP) contact times to produce peaks that correspond to directly bonded C-H and through-space dipolar-coupled C···H moieties. For Y6 crystal (Form II, **Figure 4d-f**, **Figure 5b-g** red squares), the GIPAW-DFT calculated ^{1}H and ^{13}C chemical shifts for all ^{1}H-^{13}C pairs within 1.5 Å (short-range) and within 5 Å (long-range) are overlaid with the 2D experimental data (dots in **Figure 7a**). Inter- and intramolecular C-H proximities corresponding to the experimental and simulated 2D peaks are shown in **Figure 7b**. For both the short and long-range 2D correlations, good agreement is obtained between the DFT calculated and experimental chemical shifts of alkyl groups i-iii (^{13}C, 10-45 ppm, and ^{1}H 1.0-8.0 ppm), whereas a divergence in the DFT versus experimental chemical shifts is observed for the end groups and branched sidechains. Notably, a divergence in the DFT-calculated ^{13}C chemical shifts

(50-60 ppm) compared to experimental ^{13}C NMR peaks (~55 ppm, directly bonded C-H) is observed for –NCH_2– groups (iv) of the fused-ring core (Supporting Information, **Table S5**). In addition, the experimental 2D peaks correspond to Y6 end-groups at ^{13}C (112-114 ppm) and ^{1}H (6.5-8.5 ppm) and the 2D peaks originating from the =C-H moieties bridging the fused-ring core and end-groups at ^{13}C (133-134 ppm) and ^{1}H (7.5-8.5 ppm) corroborate that the DFT-calculated chemical shifts at ^{13}C (100-106 ppm and 129-134 ppm) are slightly different, indicating the different local chemical environments in the vicinity of end groups and branched sidechains in Y6 crystals and thin films processed from CF.[3] The divergence between DFT and experimental chemical shifts is also reflected in the 2D ^{13}C-^{1}H correlation spectrum acquired with a longer CP contact time (**Figure 7a**, through-space C···H correlations). Specifically, 2D peaks shown in red boxes vii and viii (^{13}C, 113-114 ppm and ^{1}H, 1.3-2.5 ppm; ^{13}C 30-32 ppm and ^{1}H 6.5-8.5 ppm), and peaks at ^{13}C (133-134 ppm) and ^{1}H (2.5-1.3 ppm) indicate the close proximity between end groups and sidechains (**Figure 7b**), which is in line with the RDF analysis of sidechain/end group interactions (Forms II and III, **Figure 6**). In particular, the intermolecular C-F···H and C≡N···H interactions between end groups and branched sidechains (Supporting Information, **Figure S17**) are expected to contribute such 2D correlation peaks, indicating these non-covalent interactions stabilize the end-group stacking in the supramolecular structure of Y6 molecules. The long-range 2D peaks associated with ^{13}C (152-156 ppm) and ^{1}H (7.0-8.5 ppm) are ascribed to the close vicinities of quaternary/fluorinated carbon atoms and aromatic protons in the end groups; and 2D peaks from ^{13}C (152-156 ppm) and ^{1}H (3.5-1.0 ppm) are attributed to the through-space proximity between quaternary aromatic carbons and sidechain protons, which were also reflected in the 2D peaks at ^{13}C (27-33 ppm) and ^{1}H (7.0-8.0 ppm).

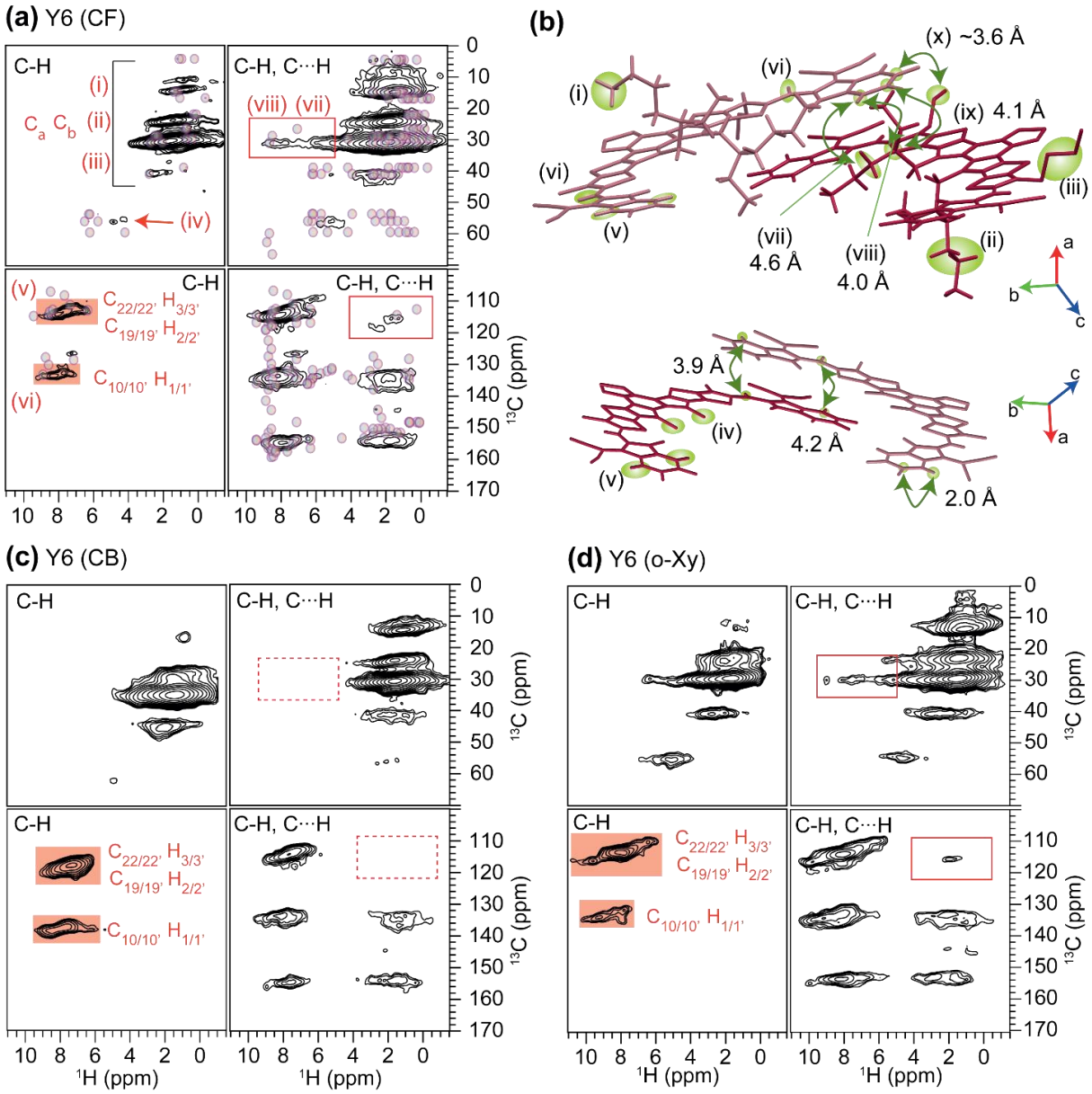

Figure 7. Solid-state 2D ^{1}H-^{13}C HETCOR spectra for neat **Y6** films processed from **(a)** CF, **(c)** CB and **(d)** *o*-XY solvents with aliphatic (top) and aromatic (bottom) regions. Spectra were acquired with 0.1 ms (left panels) and 4 ms (right panels) CP contact times, depicting the directly bonded C-H and through-space C···H interactions, respectively. The overlaid dots in **(a)** correspond to the GIPAW DFT calculated ^{1}H and ^{13}C chemical shifts of Form II crystal of Y6 (Figures 4b, 6b). In **(b)** inter- and intramolecular ^{1}H-^{13}C proximities in Form II that contribute to specific 2D peaks are indicated. Red color shaded boxes depict the directly bonded C-H correlation peaks in the end

groups. Dashed boxes indicate the 2D peaks correspond to inter- and intramolecular dipoar interactions between end-groups and alkyl sidechains of Y6 molecules. Spectra were acquired at 18.8 T (^{1}H = 800.1 MHz, ^{13}C = 201.2 MHz) spectrometer with 50 kHz MAS.

By comparison, the Y6 films processed from CB and *o*-XY exhibit different 2D peaks (**Figure 7c,d**), which are attributable to different local structures in the vicinities of end groups and sidechains-end group interactions. Although there are no crystal structures available for CB and o-XY processed Y6 molecules, analysis of experimental 2D ^{1}H-^{13}C spectra (peaks shown in red shaded regions and boxes) provides a benchmark for morphological features in Y6 thin films. The most notable of all is the broad distribution of 2D peaks associated with the end groups (C_{22}, C_{19} and C_{10}, red shaded regions) and branched sidechains attached to pyrrole ring of the core (iv), suggesting that local structures these groups are dependent on solvent processing leading to different self-assembly and thin film morphology. In the case of CB processed Y6 film, the HETCOR spectrum acquired with 0.1 ms of CP time shows a broad distribution of 2D peaks at ^{13}C (112-116 ppm) and ^{1}H (6.5-8.0 ppm), and 2D peaks associated with bridged $C_{10/10'}$-$H_{1/1'}$ moieties at ^{13}C (133-134 ppm) and ^{1}H (2.5-1.3 ppm) indicating that the different end group orientations with respect to the core. This is further corroborated by the distribution of 2D peaks between ^{13}C (55-56 ppm) and ^{1}H (3.0-7.0 ppm) associated with –NCH_2– moieties, suggesting the changes in the local structures of branched sidechains. In addition, specific 2D peaks corresponding to through-space $^{13}C^{\cdots 1}H$ contacts between end groups and sidechains do not appear in the 2D HETCOR spectrum (**Figure 7c**, dashed rectangle), further confirming the sidechain-end group contacts in the CB-processed Y6 film are different than the ones observed in Forms II and III (**Figure 6**, RDFs). For Y6 films processed from *o*-XY (**Figure 7d**), much broader distributions of 2D peaks are observed (red shaded regions); ^{13}C (110-117 ppm) and ^{1}H (6.5-9.5 ppm) originating from end

groups and at ^{13}C (130-138 ppm) and ^{1}H (7.5-9.5 ppm) originating from bridged $C_{10/10'}$-$H_{1/1'}$ moieties. However, in the 2D spectrum acquired with 4 ms of contact time, the 2D peaks corresponding to the sidechain-end group contacts are present (solid rectangle). These results are further corroborated by the analysis of ^{1}H DQ-SQ correlation spectra (Supporting Information, **Figures S16**), which show different ^{1}H DQ peaks corresponding to different local structures and intermolecular interactions in Y6 thin films processed from different solvents.

Evidently, the combined ssNMR, GIPAW-DFT and MD simulations approach identifies that the end groups and sidechains and interactions between them play an important role in governing acceptor morphology, and also provide evidence that Y6 processed from CF has improved molecular ordering and morphology than the same material processed from CB and *o*-XY. This indicates Y6 materials processed from CF, CB and o-XY solvents have key differences in molecular self-assembly and thin-film morphology. The end groups and sidechains attached to the fused-ring core adapt into different structures, thus controlling the degree of π–π overlap and 3D connectivity of Y6 molecules. In addition, C-H···π, C-H···F, C-H···N, O···F and S···F interactions, and cooperativity between them, drive self-assembly and thin-film morphology in Y6 films. Specifically, the observed differences in the experimental 2D NMR correlation peaks in Y6 processed from CB and *o*-XY compared to CF indicates the structural changes in the vicinity of sidechains and end groups. While it can be postulated that the end group and sidechain orientations in thin films may adapt different spatial and angular distributions predicted by MD simulations (**Figures 6** and **S14**), further development of the NMR crystallography approaches (iteration step, **Figure 2**) based on quantum mechanical (QM) calculations in combination with MD simulations that explicitly account for the interaction with solvent molecules and for different evaporation rates are anticipated to provide further insight into an atomic-level understanding of thin-film morphology.

Next, we extend the rationale explaining the different morphologies observed in neat Y6 films to the different BHJ morphologies and solar-cell performances of PM6:Y6 blends (step 6, **Figure 2**) processed from the same solvents. We reconcile the experimental ^{19}F analysis (**Figure 3**) with NMR crystallography and MD simulations (**Figures 4-7**) to provide molecular-level insight into the packing interactions in PM6:Y6 blends. While the optimal PM6:Y6 BHJ morphology processed from CF favors charge generation and extraction, the dramatically lower performance of the same blend processed from CB and *o*-XY can be linked to the acceptor morphology, especially the differences in the interactions between the end groups, backbone, and sidechains. This is further corroborated by analyzing and comparing the 2D ^{1}H-^{13}C HETCOR spectra of PM6:Y6 BHJ blend films with the spectra of the neat materials, as shown in **Figure 8** below.

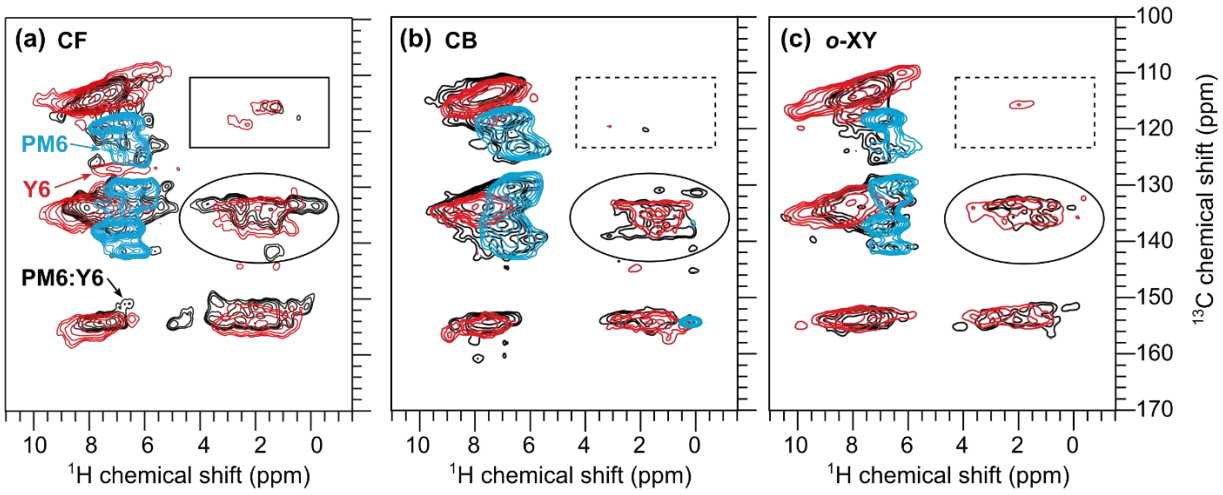

Figure 8. Aromatic regions of the solid-state 2D ^{1}H-^{13}C HETCOR spectra of PM6 (turquoise), Y6 (red) and PM6:Y6 blends (black) cast from **(a)** CF, **(b)** CB, and **(c)** *o*-XY solvents. All 2D spectra were acquired at high a field and fast MAS (18.8 T, 50 kHz MAS) and at 298 K with CP contact time of 4ms. 2D HETCOR spectra corresponding to directly bonded C-H and through-space C···H correlations acquired with CP contact times of 0.1 ms and 4 ms together with the analysis are shown in Supporting Information (**Figures S18** and **S19**).

Figure 8 compares 2D HETCOR spectra of neat PM6, Y6 and PM6:Y6 blends processed from CF, CB, and *o*-XY solvents. The signals corresponding to the neat Y6 (red traces) and PM6 (turquoise traces) films are very similar to those in the BHJ blends (black traces), indicating well-defined phase separation of Y6 and PM6 domains in the BHJ morphology, with few D-A interactions contributing to changes in the signals from the neat materials. However, the distribution of 2D correlation peaks associated with the end groups of Y6 molecules ($^{13}C_{10/10'}$ 110 – 118 ppm, $H_{1/1'}$ 7.5-8.5 ppm, and $^{13}C_{19/19'}$ 130 – 138 ppm, $H_{2/2'}$ 7.5-8.5 ppm, as depicted in the red boxes in **Figure 7**) in the blend films cast from CF is narrower than those cast from CB and *o*-XY, providing further evidence that Y6 films prepared from CF are more ordered by means of end groups π–π stacking (see **Figure 6b**, green sphere) and end groups/sidechain interactions (see **Figure 6b**, blue sphere). Locally disordered end groups, especially tilting of end groups with respect to the fused-ring core, cause perturbation of intermolecular interactions between the π–π stacked end groups, and between the end group and branched sidechains. This is further corroborated by the different frequency distributions and intensities of 2D ^{1}H-^{13}C peaks depicted in solid and dashed rectangles and solid ovals (**Figure 8**), which correspond to the inter- and intramolecular interactions between the end groups and sidechains (both linear and branched) at sub-nm distances in Y6 molecules. These 2D peaks allow two different aspects to be inspected: changes in Y6 morphology in neat films and blends (red versus black spectra in each blend) and the impact of solvent processing on the Y6 morphology in blend films (red and black spectra of CF, CB and *o*-XY processed blends), whereby CB and *o*-XY processed blends exhibit significantly different 2D peaks (boxes and ovals) than the CF processed BHJ blend. A complete analysis of the 2D HETCOR spectra, including the aliphatic ^{13}C regions of PM6:Y6 blends processed from different solvents is presented in the Supporting Information (**Figures S18** and **S19**). In the case of *o*-XY processed blend, a significant change in the 2D ^{1}H-^{13}C correlation peaks ($^{13}C_{19/19'}$ and $^{13}C_{22/22'}$

~114 ppm, ^{1}H 1-3 ppm, and ^{1}H 7.5-6.5 ppm) indicates the changes in the local structures and much weaker dipolar interactions between end groups and sidechains of Y6 molecules (**Figure 8c,** box). In addition, the relatively weak intensity 2D signals in the range of ^{13}C (130-156 ppm) and ^{1}H (1-3 ppm) in the CB and o-XY processed blends than the CF processed blend indicate the weak dipolar interactions between end groups and sidechains of Y6 molecules. Detailed analysis of ^{1}H and ^{13}C chemical shift displacements in neat compounds and BHJ blends can also be carried out by acquiring and comparing the ^{1}H-^{13}C 2D HETCOR spectra at several CP contact times which allow the 2D peaks corresponding to short- and long-range interactions to be distinguished and identified, although this approach is time demanding and necessitates extensive data analysis. For fluorinated donor and acceptor moieties such as PM6 and Y6, 2D heteronuclear ^{13}C-^{19}F correlation and ^{19}F-^{1}H correlation experiments provide further insights into inter- and intramolecular backbone-backbone and backbone-sidechain interactions.[50,68,69] Despite the high sensitivity of ^{19}F NMR (100% natural abundance) and substantial chemical shift range, such experiments usually require specialized triple-resonance H-F-X (X=^{13}C) NMR probes. In addition, the sensitivity of 2D ^{13}C-^{19}F correlation experiments relies on relatively weak ^{13}C-^{19}F dipolar interactions between flexible sidechains and backbone moieties. This is further exacerbated by the minuscule concentrations of ^{19}F nuclei in donor and acceptor molecules (1.3 atom% in PM6, 2.1 atom% in Y6 and ~1.8 atom% in 1:2 PM6:Y6 blend), longer relaxation delays associated with ^{19}F than ^{1}H, and low sample concentrations (often < 5 mg of thin films used for fast MAS experiments). In 2D ^{13}C-^{19}F heteronuclear correlation spectra of neat Y6 and PM6:Y6 blends (Supporting Information, **Figure S20**), 2D correlation peaks corresponding to directly bonded ^{19}F-^{13}C sites are observed but the 2D peaks associated with long-range interactions between NFA end groups and sidechains are too weak to be detected. Overall, this analysis suggests that a focus on end group and sidechain engineering is the path forward to develop NFAs with improved morphology in thin films and BHJ

blends. Targeting materials that have strong interactions between the end groups and the sidechains will lead to less sensitivity to processing conditions, thus enabling stable and efficient OSC blends. Research along this direction has already enabled high-performance NFA organic solar cells with PCE values reaching and exceeding 19%,[2] and this trend is expected to continue. Thus, an accurate understanding of the self-assembly and intermolecular interactions enabled by comprehensive NMR crystallography and modeling approach will certainly expedite chemical design strategies for NFAs. However, the overall performance of solar cells depends on multiple factors such as degree of disorder of the active layer, phase purity, and dynamics of intra- and inter-molecular motions. Thus, experimental techniques and computational simulations that comprehensively consider these factors are called for in order to improve the robustness of the NMR crystallography approach and establish rigorous structure-processing-property relationships. Synthetic approaches that enable the growth of NFAs single crystals suitable for X-ray diffraction studies in conjunction with high resolution 2D ssNMR characterization (^{1}H-^{1}H and ^{1}H-X correlation experiments, X=^{19}F, ^{13}C, ^{15}N) and modelling techniques would help resolve the local morphological differences in BHJ blends, further widening the scope of the NMR crystallography approach (Figure 2) to develop structure-property relationships in organic solar cells. In addition, the role of dynamic motion of donor and acceptor molecules on the optoelectronic properties cannot be ignored. Dynamics information obtained from ssNMR techniques,[70-72] ultrafast spectroscopy and molecular modelling may provide additional insights,[73-75] although the different timescales associated these characterization techniques and photophysical events makes it less straightforward to draw conclusions about structure-dynamics-property correlations in NFA-based BHJ solar cells.

3. Conclusion

This study demonstrates an experimental approach to resolve atomic-scale interactions that drive molecular self-assembly in BHJ OSCs. Additionally, we develop a framework for understanding how these interactions govern the overall solar cell device performance. In particular, the combined results from ssNMR, X-ray crystallography, DFT, and MD simulations highlight key differences in the packing of Y6 molecules in PM6:Y6 blends cast from different solvents. The choice of solvent has a large impact on the resulting solid-state interactions between the Y6 end groups and the aliphatic sidechains, both within the same molecule and from neighboring Y6 molecules. These different interactions manifest in morphological differences between the blends that ultimately influence the device performance, which is seen in the large variation in PCEs. Thus, new acceptor materials derived from the Y6 structure should focus on enhancing these end group/sidechain interactions to enforce greater planarity and structural uniformity in Y6 domains, which will ultimately lead to increased performance.

In a more general context, the methodology shown here is widely applicable for understanding the complex chemical, morphological, and structural relationships that govern the physics of organic semiconductor devices. The observed differences in bulk properties, such as device performance or absorption characteristics, can be investigated using NMR crystallography, modeling, and other general characterization techniques. By interpreting the data from each step of the process using the results from the other steps, specific understandings of the underlying fundamental processes is reached. The proposed approach has some drawbacks, for example, the compositional and structural heterogeneity of BHJ blends is a major bottleneck to obtain accurate ssNMR-based structure and dynamics information due to the spectral overlap issues. It can be envisaged that the further optimization of NMR crystallography approach by means of advanced ssNMR characterization, single crystal XRD analysis of NFAs and molecular modelling leads to better

resolution of molecular self-assembly and packing interactions in a BHJ morphology. In addition, insights from dynamics studies based on ssNMR, ultrafast spectroscopy and MD simulations are expected to help to understand dynamics-property relationships in BHJ solar cells.

Supporting Information

Supporting Information is available from the Wiley Online Library or from the authors. GIPAW optimized crystal structures (CIF format) are available from the authors upon a reasonable request.

Acknowledgements

B.R.L. and P.R. contributed equally to this work. B.R.L., N.S., S.Y., S.C, T-Q.N., T.W., G.K., V.C., and J.L.B. gratefully acknowledge the financial support of the United States Department of the Navy, Office of Naval Research (Research Awards No. N00014-21-1-2181 and N00014-21-1-2182). T.W., G.K., V.C., and J.L.B. thank the DOD High Performance Computing Modernization Program for computational resources. Z.D. thanks the Air Force Office of Scientific Research (Grant No. FA9550-19-1-0348) for the financial support. G.N.M.R. acknowledges the financial support from University of Lille, IR-RMN-THC FR-3050 CNRS, and EU-H2020 (Grant No. 795091) for conducting ssNMR experiments. The computational resources were partially provided by the Polish Infrastructure for Supporting Computational Science in the European Research Space (PL-Grid). We would like to personally thank the authors of reference [65] for their contributions to the MagresView and MagresPython tools for visualizing and processing NMR crystallography data.

Conflicts of Interest

The authors declare no conflicts of interest.

Data Availability Statement

The data in support of these findings are available from the corresponding authors upon request.

Author ORCiDs

B. R. Luginbuhl	0000-0001-5062-0994
P. Raval	0000-0003-2991-4490
T. Pawlak	0000-0002-0350-6395
Z. Du	0000-0001-6814-8317
T. Wang	0000-0002-5027-1541
G. Kupgan	0000-0001-8163-9786
N. Schopp	0000-0002-6920-0241
S. Chae	0000-0002-0655-7577
S. Yoon	0000-0002-8052-1804
A. Yi	0000-0003-2001-2828
H. J. Kim	0000-0002-9725-8598
V. Coropceanu	0000-0003-1693-2315
J-L. Brédas	0000-0001-7278-4471
T-Q. Nguyen	0000-0002-8364-7517
G. N. Manjunatha Reddy	0000-0002-8283-2462

Received: {will be filled in by the editorial staff}
Revised: {will be filled in by the editorial staff}
Published online: {will be filled in by the editorial staff}

References

[1] Q. Liu, Y. Jiang, K. Jin, J. Qin, J. Xu, W. Li, J. Xiong, J. Liu, Z. Xiao, K. Sun, S. Yang, X. Zhang, L. Ding, *Science Bulletin* **2020**, *65*, 272.

[2] C. Li, J. Zhou, J. Song, J. Xu, H. Zhang, X. Zhang, J. Guo, L. Zhu, D. Wei, G. Han, J. Min, Y. Zhang, Z. Xie, Y. Yi, H. Yan, F. Gao, F. Liu, Y. Sun, *Nat Energy* **2021**, *6*, 605.

[3] J. Yuan, Y. Zhang, L. Zhou, G. Zhang, H.-L. Yip, T.-K. Lau, X. Lu, C. Zhu, H. Peng, P. A. Johnson, M. Leclerc, Y. Cao, J. Ulanski, Y. Li, Y. Zou, *Joule* **2019**, *3*, 1140.

[4] P. Cheng, Y. Yang, *Acc. Chem. Res.* **2020**, *53*, 1218.

[5] A. Karki, J. Vollbrecht, A. L. Dixon, N. Schopp, M. Schrock, G. N. M. Reddy, T. Nguyen, *Adv. Mater.* **2019**, *31*, 1903868.

[6] G. Zhang, X.-K. Chen, J. Xiao, P. C. Y. Chow, M. Ren, G. Kupgan, X. Jiao, C. C. S. Chan, X. Du, R. Xia, Z. Chen, J. Yuan, Y. Zhang, S. Zhang, Y. Liu, Y. Zou, H. Yan, K. S. Wong, V. Coropceanu, N. Li, C. J. Brabec, J.-L. Bredas, H.-L. Yip, Y. Cao, *Nat Commun* **2020**, *11*, 3943.

[7] Y. Cui, H. Yao, J. Zhang, K. Xian, T. Zhang, L. Hong, Y. Wang, Y. Xu, K. Ma, C. An, C. He, Z. Wei, F. Gao, J. Hou, *Adv. Mater.* **2020**, *32*, 1908205.

[8] Q. Guo, Q. Guo, Y. Geng, A. Tang, M. Zhang, M. Du, X. Sun, E. Zhou, *Mater. Chem. Front.* **2021**, 3257.

[9] W. Zhu, A. P. Spencer, S. Mukherjee, J. M. Alzola, V. K. Sangwan, S. H. Amsterdam, S. M. Swick, L. O. Jones, M. C. Heiber, A. A. Herzing, G. Li, C. L. Stern, D. M. DeLongchamp, K. L. Kohlstedt, M. C. Hersam, G. C. Schatz, M. R. Wasielewski, L. X. Chen, A. Facchetti, T. J. Marks, *J. Am. Chem. Soc.* **2020**, *142*, 14532.

[10] L. Zhu, M. Zhang, G. Zhou, T. Hao, J. Xu, J. Wang, C. Qiu, N. Prine, J. Ali, W. Feng, X. Gu, Z. Ma, Z. Tang, H. Zhu, L. Ying, Y. Zhang, F. Liu, *Adv. Energy Mater.* **2020**, *10*, 1904234.

[11] C. Xiao, C. Li, F. Liu, L. Zhang, W. Li, *J. Mater. Chem. C* **2020**, *8*, 5.

[12] Z. Huang, D. Ouyang, R. Ma, W. Wu, V. A. L. Roy, W. C. H. Choy, *Advanced Functional Materials* **2019**, *29*, 1904684.

[13] J. Dong, J. Guo, X. Wang, P. Dong, Z. Wang, Y. Zhou, Y. Miao, B. Zhao, Y. Hao, H. Wang, B. Xu, S. Yin, *ACS Appl. Mater. Interfaces* **2020**, *12*, 46373.

[14] S. Chen, L. Liu, X. Gao, Y. Hua, L. Peng, Y. Zhang, L. Yang, Y. Tan, F. He, H. Xia, *Nat Commun* **2020**, *11*, 4651.

[15] B. Liu, Y. Wang, P. Chen, X. Zhang, H. Sun, Y. Tang, Q. Liao, J. Huang, H. Wang, H. Meng, X. Guo, *ACS Appl. Mater. Interfaces* **2019**, *11*, 33505.

[16] Q. Yang, S. Yu, P. Fu, W. Yu, Y. Liu, X. Liu, Z. Feng, X. Guo, C. Li, *Adv. Funct. Mater.* **2020**, *30*, 1910205.

[17] J. Yao, B. Qiu, Z.-G. Zhang, L. Xue, R. Wang, C. Zhang, S. Chen, Q. Zhou, C. Sun, C. Yang, M. Xiao, L. Meng, Y. Li, *Nat Commun* **2020**, *11*, 2726.

[18] S.-H. Lee, S.-J. Ko, S. H. Eom, H. Kim, D. W. Kim, C. Lee, S. C. Yoon, *ACS Appl. Mater. Interfaces* **2020**, *12*, 14244.

[19] H. Liu, Z. Ma, R. Yu, H. Gao, J. Lin, T. Hayat, A. Alsaedi, Z. Tan, *Mater. Chem. Front.* **2020**, *4*, 2995.

[20] M. Zeng, X. Wang, R. Ma, W. Zhu, Y. Li, Z. Chen, J. Zhou, W. Li, T. Liu, Z. He, H. Yan, F. Huang, Y. Cao, *Advanced Energy Materials* **2020**, *10*, 8.

[21] W. Zhang, W. Song, J. Huang, L. Huang, T. Yan, J. Ge, R. Peng, Z. Ge, *J. Mater. Chem. A* **2019**, *7*, 22021.

[22] Y. Luo, S. Fang, N. Zheng, L. Liu, F. Würthner, Z. Xie, *ACS Appl. Energy Mater.* **2020**, *3*, 1694.

[23] C. Hou, H. Yu, *J. Mater. Chem. C* **2020**, *8*, 4169.

[24] K. Yang, S. Chen, J. Fu, S. Jung, J. Ye, Z. Kan, C. Hu, C. Yang, Z. Xiao, S. Lu, K. Sun, *ACS Appl. Mater. Interfaces* **2020**, *12*, 30954.

[25] Z. Zhang, Z. Zhang, Y. Yu, B. Zhao, S. Li, J. Zhang, S. Tan, *Journal of Energy Chemistry* **2020**, *47*, 196.

[26] H. Tang, Z. Liu, Z. Hu, Y. Liang, F. Huang, Y. Cao, *Sci. China Chem.* **2020**, *63*, 802.

[27] H. Jiang, T. Li, X. Han, X. Guo, B. Jia, K. Liu, H. Cao, Y. Lin, M. Zhang, Y. Li, X. Zhan, *ACS Appl. Energy Mater.* **2020**, *3*, 1111.

[28] R. Peng, T. Yan, J. Chen, S. Yang, Z. Ge, M. Wang, *Advanced Electronic Materials* **2020**, *6*, 1901245.

[29] Y. Ge, L. Hu, L. Zhang, Q. Fu, G. Xu, Z. Xing, L. Huang, W. Zhou, Y. Chen, *ACS Appl. Mater. Interfaces* **2020**, *12*, 10706.

[30] H.-W. Cheng, P. Raghunath, K. Wang, P. Cheng, T. Haung, Q. Wu, J. Yuan, Y.-C. Lin, H.-C. Wang, Y. Zou, Z.-K. Wang, M. C. Lin, K.-H. Wei, Y. Yang, *Nano Lett.* **2020**, *20*, 715.

[31] F. Pan, C. Sun, Y. Li, D. Tang, Y. Zou, X. Li, S. Bai, X. Wei, M. Lv, X. Chen, Y. Li, *Energy Environ. Sci.* **2019**, *12*, 3400.

[32] Z.-C. Wen, H. Yin, X.-T. Hao, *Surfaces and Interfaces* **2021**, *23*, 100921.

[33] A. Karki, A. J. Gillett, R. H. Friend, T. Nguyen, *Adv. Energy Mater.* **2021**, *11*, 2003441.

[34] T. M. Clarke, J. R. Durrant, *Chem. Rev.* **2010**, *110*, 6736.

[35] S. D. Collins, N. A. Ran, M. C. Heiber, T.-Q. Nguyen, *Adv. Energy Mater.* **2017**, *7*, 1602242.

[36] T. L. Benanti, D. Venkataraman, *Photosynth Res* **2006**, *87*, 73.

[37] S. Rafique, S. M. Abdullah, K. Sulaiman, M. Iwamoto, *Renewable and Sustainable Energy Reviews* **2018**, *84*, 43.

[38] M. Jung, D. Seo, K. Kwak, A. Kim, W. Cha, H. Kim, Y. Yoon, M. J. Ko, D.-K. Lee, J. Y. Kim, H. J. Son, B. Kim, *Dyes and Pigments* **2015**, *115*, 23.

[39] L. Yang, X. Song, J. Yu, H. Wang, Z. Zhang, R. Geng, J. Cao, D. Baran, W. Tang, *J. Mater. Chem. A* **2019**, *7*, 22279.

[40] J. Zhang, H. S. Tan, X. Guo, A. Facchetti, H. Yan, *Nat Energy* **2018**, *3*, 720.

[41] U. Vongsaysy, D. M. Bassani, L. Servant, B. Pavageau, G. Wantz, H. Aziz, *J. Photon. Energy* **2014**, *4*, 040998.

[42] A. Karki, J. Vollbrecht, A. J. Gillett, S. S. Xiao, Y. Yang, Z. Peng, N. Schopp, A. L. Dixon, S. Yoon, M. Schrock, H. Ade, G. N. M. Reddy, R. H. Friend, T.-Q. Nguyen, *Energy Environ. Sci.* **2020**, *13*, 3679.

[43] V. Vohra, K. Kawashima, T. Kakara, T. Koganezawa, I. Osaka, K. Takimiya, H. Murata, *Nature Photon* **2015**, *9*, 403.

[44] J. R. Tumbleston, B. A. Collins, L. Yang, A. C. Stuart, E. Gann, W. Ma, W. You, H. Ade, *Nature Photon* **2014**, *8*, 385.

[45] M. Seifrid, G. N. M. Reddy, B. F. Chmelka, G. C. Bazan, *Nat Rev Mater* **2020**, *5*, 910.

[46] K. R. Graham, C. Cabanetos, J. P. Jahnke, M. N. Idso, A. El Labban, G. O. Ngongang Ndjawa, T. Heumueller, K. Vandewal, A. Salleo, B. F. Chmelka, A. Amassian, P. M. Beaujuge, M. D. McGehee, *J. Am. Chem. Soc.* **2014**, *136*, 9608.

[47] R. C. Nieuwendaal, C. R. Snyder, R. J. Kline, E. K. Lin, D. L. VanderHart, D. M. DeLongchamp, *Chem. Mater.* **2010**, *22*, 2930.

[48] D. Dudenko, A. Kiersnowski, J. Shu, W. Pisula, D. Sebastiani, H. W. Spiess, M. R. Hansen, *Angew. Chem. Int. Ed.* **2012**, *51*, 11068.

[49] H. N. Tsao, D. M. Cho, I. Park, M. R. Hansen, A. Mavrinskiy, D. Y. Yoon, R. Graf, W. Pisula, H. W. Spiess, K. Müllen, *J. Am. Chem. Soc.* **2011**, *133*, 2605.

[50] B. Yurash, D. Leifert, G. N. M. Reddy, D. X. Cao, S. Biberger, V. V. Brus, M. Seifrid, P. J. Santiago, A. Köhler, B. F. Chmelka, G. C. Bazan, T.-Q. Nguyen, *Chem. Mater.* **2019**, *31*, 6715.

[51] M. T. Seifrid, G. N. M. Reddy, C. Zhou, B. F. Chmelka, G. C. Bazan, *J. Am. Chem. Soc.* **2019**, *141*, 5078.

[52] A. Karki, G. A. H. Wetzelaer, G. N. M. Reddy, V. Nádaždy, M. Seifrid, F. Schauer, G. C. Bazan, B. F. Chmelka, P. W. M. Blom, T. Nguyen, *Adv. Funct. Mater.* **2019**, *29*, 1901109.

[53] Z. Du, M. Mainville, J. Vollbrecht, A. L. Dixon, N. Schopp, M. Schrock, Z. Peng, J. Huang, S. Chae, H. Ade, M. Leclerc, G. N. M. Reddy, T.-Q. Nguyen, *Sol. RRL* **2021**, 2100213.

[54] C. E. Hughes, G. N. M. Reddy, S. Masiero, S. P. Brown, P. A. Williams, K. D. M. Harris, *Chem. Sci.* **2017**, *8*, 3971.

[55] M. Cordova, M. Balodis, A. Hofstetter, F. Paruzzo, S. O. Nilsson Lill, E. S. E. Eriksson, P. Berruyer, B. Simões de Almeida, M. J. Quayle, S. T. Norberg, A. Svensk Ankarberg, S. Schantz, L. Emsley, *Nat Commun* **2021**, *12*, 2964.

[56] N. C. Miller, E. Cho, M. J. N. Junk, R. Gysel, C. Risko, D. Kim, S. Sweetnam, C. E. Miller, L. J. Richter, R. J. Kline, M. Heeney, I. McCulloch, A. Amassian, D. Acevedo-Feliz, C. Knox, M. R. Hansen, D. Dudenko, B. F. Chmelka, M. F. Toney, J.-L. Brédas, M. D. McGehee, *Adv. Mater.* **2012**, *24*, 6071.

[57] X. Shen, W. Hu, T. P. Russell, *Macromolecules* **2016**, *49*, 4501.

[58] S. R. Chaudhari, J. M. Griffin, K. Broch, A. Lesage, V. Lemaur, D. Dudenko, Y. Olivier, H. Sirringhaus, L. Emsley, C. P. Grey, *Chem. Sci.* **2017**, *8*, 3126.

[59] C. Wang, K. Nakano, H. F. Lee, Y. Chen, Y.-L. Hong, Y. Nishiyama, K. Tajima, *Angew. Chem. Int. Ed.* **2018**, *57*, 7034.

[60] Y. Wu, Q. Hu, P. Fan, Y. Jiang, W. Zhong, W. Hu, T. P. Russell, *J. Phys. Chem. C* **2021**, 125, 15863.

[61] J. Wu, J. Lee, Y.-C. Chin, H. Yao, H. Cha, J. Luke, J. Hou, J.-S. Kim, J. R. Durrant, *Energy Environ. Sci.* **2020**, *13*, 2422.

[62] P. Hodgkinson, *Progress in Nuclear Magnetic Resonance Spectroscopy* **2020**, *118–119*, 10.

[63] G. N. M. Reddy, A. Marsh, J. T. Davis, S. Masiero, S. P. Brown, *Crystal Growth & Design* **2015**, *15*, 5945.

[64] A. L. Webber, S. Masiero, S. Pieraccini, J. C. Burley, A. S. Tatton, D. Iuga, T. N. Pham, G. P. Spada, S. P. Brown, *J. Am. Chem. Soc.* **2011**, *133*, 19777.

[65] S. Sturniolo, T. F. G. Green, R. M. Hanson, M. Zilka, K. Refson, P. Hodgkinson, S. P. Brown, J. R. Yates, *Solid State Nucl. Mag.* **2016**, *78*, 64.

[66] C. J. Pickard, F. Mauri, *Phys. Rev. B* **2001**, *63*, 245101.

[67] R. K. Harris, P. Hodgkinson, C. J. Pickard, J. R. Yates, V. Zorin, *Magn. Reson. Chem.* **2007**, *45*, S174.

[68] M. Murakami, K. Matsumoto, R. Hagiwara, Y. Matsuo, *Carbon* **2018**, *138*, 179.

[69] Q. Wang, S. Böckmann, F. Günther, M. Streiter, M. Zerson, A. D. Scaccabarozzi, W. L. Tan, H. Komber, C. Deibel, R. Magerle, S. Gemming, C. R. McNeill, M. Caironi, M. R. Hansen, M. Sommer, *Chem. Mater.* **2021**, *33*, 2635.

[70] M. R. Hansen, R.Graf, H. W. Spiess, *Chem. Rev.* **2016,** *116*, 1272

[71] M. R. Hansen, X. Feng, V. Macho, K. Müllen, H. W. Spiess, and G. Floudas, *Phys. Rev. Lett.* **2011**, 107, 257801

[72] M. R. Hansen, T. Schnitzler, W. Pisula, R. Graf, K. Müllen, H.W. Spiess, *Angew. Chem. Int. Ed.* **2009**, 48, 4621

[73] F. Etzold, I. A. Howard, N. Forler, D. M. Cho, M. Meister, H. Mangold, J. Shu, M. R. Hansen, K. Müllen, F. Laquai, *J. Am. Chem. Soc.* **2012**, 134, 10569

[74] F. Etzold, I. A. Howard, N. Forler, A. Melnyk, D.Andrienko, M. R Hansen, F. Laquai, *Energy Environ. Sci.* **2015**, 8, 1511

[75] A. Karki, A. j. Gillett, R. H. Friend, T.-Q. Nguyen, *Adv. Energy Mater.* **2021**, 11, 2003441

Resolving atomic-scale interactions in non-fullerene acceptor organic solar cells with solid-state NMR spectroscopy, crystallographic modelling, and molecular dynamics simulations

B. R. L., P. R., T. P., Z. D., T. W., G. K., N. S., S. C., S. Y., A. Y., H. J. K., V. C., J-L. B., T-Q. N., G. N. M. R.

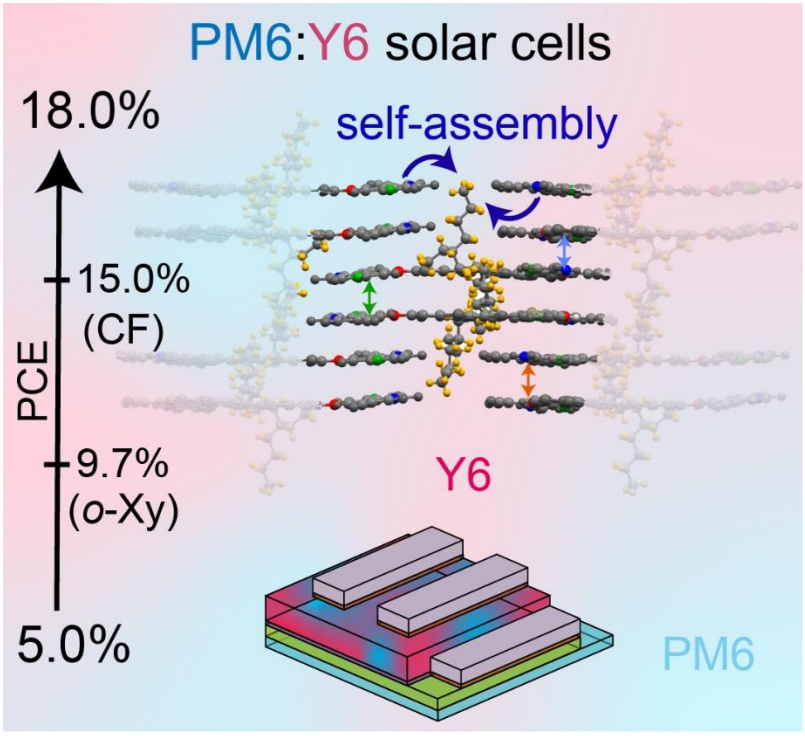

SHORT ABSTRACT: The combined results from solid-state NMR, crystallography and modelling techniques highlight key differences in the Y6 morphology in PM6:Y6 blends cast from different solvents, which lead to different power conversion efficiencies in solar cells. By interpreting the experimental data step-by-step and using the results from each step, a more complete understanding of the underlying fundamental processes is reached.